Article

An Innovative Curvelet-only-Based Approach for Automated Change Detection in Multi-Temporal SAR Imagery

Andreas Schmitt *, Birgit Wessel and Achim Roth

Land Surface Applications (LAX), German Remote Sensing Data Center (DFD), German Aerospace Center (DLR), Oberpfaffenhofen, D-82234 Wessling, Germany;
E-Mails: birgit.wessel@dlr.de (B.W.); achim.roth@dlr.de (A.R.)

* Author to whom correspondence should be addressed; E-Mail: andreas.schmitt@dlr.de;
Tel.: +49-815-328-3341; Fax: +49-815-328-1458.

Abstract: This paper presents a novel approach for automated image comparison and robust change detection from noisy imagery, such as synthetic aperture radar (SAR) amplitude images. Instead of comparing pixel values and/or pre-classified features this approach clearly highlights structural changes without any preceding segmentation or classification step. The crucial point is the use of the Curvelet transform in order to express the image as composition of several structures instead of numerous individual pixels. Differentiating these structures and weighting their impact according to the image statistics produces a smooth, but detail-preserved change image. The Curvelet-based approach is validated by the standard technique for SAR change detection, the log-ratio with and without additional gamma maximum-a-posteriori (GMAP) speckle filtering, and by the results of human interpreters. The validation proves that the new technique can easily compete with these automated as well as visual interpretation techniques. Finally, a sequence of TerraSAR-X High Resolution Spotlight images of a factory building construction site near Ludwigshafen (Germany) is processed in order to identify single construction stages by the time of the (dis-)appearance of certain objects. Hence, the complete construction monitoring of the whole building and its surroundings becomes feasible.

1. Introduction

With the rapidly increasing importance of time series in remote sensing applications the need for robust change detection on multi-temporal acquisitions is increasing likewise. Synthetic Aperture Radar on the one hand is an ideal sensor because of its capability of illumination and weather independent image acquisition. On the other hand, the high noise content due to the presence of deterministic multiplicative and stochastic additive noise complicates image interpretation and, thus, image comparison as well. Robust image comparison—often referred to as change detection—is the key to any monitoring purpose in the context of remote sensing applications. Visual image comparison by a human interpreter discards because of the high amount of data. Therefore, automated methods have to be developed that extract distinct changes out of a huge amount of data points.

Concerning the field of application three types can be distinguished according to [1]: land cover monitoring, land use monitoring, and damage mapping. While land cover monitoring cares for seasonal changes in vegetated areas (mainly slow changes in large areas), land use monitoring addresses human activities that change the environment (more structured changes in shorter time periods). Damage assessment focusses on sudden changes caused by natural disasters that can adopt any geometric form. In this context, our Curvelet-based approach is designed especially for land use monitoring and damage assessment because of its sensitivity for stronger structural changes as expected with anthropogenic activities, though seasonal changes can be analyzed as well.

Regarding the change detection algorithm the data base for making the decision "change" or "no change" plays an important role. Again three types have been mentioned in literature so far: pre-, para-, and post-classification techniques [1] at which the classification can be supervised or unsupervised depending on whether training areas are available or not. Starting with the latter ones, both input images are classified separately and the resulting pixel- or segment-based features are compared [2]. This approach requires a most reliable feature identification algorithm in order to avoid false alarms [3]. The term para-classification change detection denotes the joint classification of an image pair, thus the input images are segmented and classified simultaneously. As the identification of similarities and differences is performed during the classification process the reliability increases slightly. The pre-classification techniques comprise all approaches that detect changes from the image data directly before any segmentation or classification step is performed. All of the following approaches—including the Curvelet-based change detection—can be numbered among this group.

The crucial point of the direct image comparison is the noise handling. Due to SAR image characteristics the mixture of additive and multiplicative noise contributions cause a very high false alarm rate when comparing two images pixel by pixel. There are different ways to overcome this problem. One may add further information layers to the mostly used logarithmic intensity quotient (briefly "log-ratio")—like correlation [4] or coherence [5]—or take into account larger patches to feed the statistical models [3]. In this context a wide range of so-called random field algorithms—iteratively trying to find an optimal solution for a given image subset—has been developed and published [1,6,7]. Others envisage a sophisticated statistical modeling of the noise components based on common speckle models [8–11] often requiring a higher number of looks and, thus, a reduced geometric resolution. A quite new and still more theoretical way is the comparison of a real-noise affected-SAR image with a synthetic-quasi noise free- reference in order to simplify the noise model. With respect to

the field of application this synthetic reference image is either simulated using a high resolution DEM for urban applications [12,13] or combined out of a large number of multi-aspect SAR acquisitions (e.g., multi-temporal and different imaging geometries) to balance seasonal, as well as SAR illumination effects in land cover monitoring [14]. As those methods are very specialized in a certain field of application, they are quite often restricted to their original purpose.

In order to develop more flexible change detection tools the logarithmic intensity quotient was investigated in terms of scale-dependent characteristics by the help of the wavelet transform [15,16]. Though using different statistical instruments, the crucial point that mostly is carried out by interactive parameter tuning still is the selection of the appropriate scale for the reliable change detection. To this effect, the wavelet-based methods are similar to the adaptive filtering of the difference image already mentioned in [3]. The common problem of these methods is the detection of structural changes in an image—the logarithmic intensity quotient—that has no apparent structures due to the very high noise content. Therefore, the Curvelet-based approach starts with the detection of structures in the original images and proceeds with their comparison in the coefficient domain, but without any classification step common to para- and post-classification change detection algorithms. The multi-scale and multi-directional image description by the help of Curvelets is designed to describe linear features in an optimum way [17]. Significant features are indicated by high coefficient amplitudes. Hence, in our approach the Curvelet representation only has to be reduced to a subset of the strongest coefficients which equals an image compression. Occurring artifacts are then suppressed by introducing a weighting function that smoothes the transition from rejected to maintained coefficients. Though, the output image still is continuous, it easily can be classified into significant and non-significant changes by simple thresholding the strength of the changes because unstructured noise is already completely removed.

Recently, another study dealing with time series and Curvelets was published [18]. Although the input data as well as the tools look similar at first glance, there are striking differences that should be mentioned in the following. The aim of [18] is to reduce a large amount of multi-temporal images to a minimum layer stack containing all the distinct changes occurring in the test site while our approach is designed for the robust and reliable comparison of two images, thus, it is a pure image processing. The Curvelet and Wavelet coefficients in [18] are exclusively used to highlight structures in the images. Instead of comparing the coefficients directly and independently of their scale, orientation, or location—like we do—only the similarity of their distributions is checked for every sub-band separately which seems to be very intricate. Beyond that, the change itself is computed on pixel level—in the traditional way—in [18], while we transfer for the first time ever the image comparison completely to the coefficient domain of an alternative image representation. Although the feature selection in [18] and our image enhancement step perform in a comparative way—the reduction of the number of Curvelet coefficients—our approach excels in the use of a sophisticated weighting function for efficient artifact suppression. Thus, we are able to present for the first time an innovative Curvelet-only-based approach for image comparison and subsequent image enhancement that turns out to be an ideal tool for change detection in multi-temporal SAR imagery.

Our paper is organized as follows: In Section 2 the methodology comprising Curvelet-based change measure as well as the Curvelet-based image enhancement is introduced. The actual work flow and its validation towards standard techniques and human interpreters are summarized in Section 3. Section 4

gives a practical example for the use of our Curvelet-based change detection. The conclusions can be found in Section 5.

2. Methodology

The methodology section consists of two steps: at first the Curvelet-based image comparison (*i.e.*, the generation of change images) and at second the Curvelet-based image enhancement, thus, the suppression of noise without producing artifacts.

2.1. Curvelet-Based Image Comparison

The idea of novel image representations like Curvelets or Wavelets is to describe apparent structures directly instead of storing single pixel values that might form a structure together with a group of their neighboring pixels at second glance. Out of the wide choice of image descriptors the Curvelet transform [17] was chosen. At first, it decomposes the image into linear structures with arbitrary orientation like they can be found in SAR images of urban areas [19]. Secondly, being defined in the continuous domain and transported to the discrete domain afterwards—while retaining high redundancy and, thus, guaranteeing sufficient sampling—it is more resistant towards noise then other—critically sampled—decompositions [20]. The principles of the Curvelet representation are shortly presented in the following. Then, the Curvelet representation is introduced for image comparison. Finally, the coefficient distribution of the resulting image is investigated.

2.1.1. Curvelet-Based Image Description

Instead of interpreting the image as carpet of numerous individual pixels most novel image representations decompose the image into a sequence of structures. In the case of Curvelets the basic structure is derived from a ridge-like form—called Ridgelet [17]. These functions do not explicitly describe the image content, but they describe the deviation from the mean value over the whole image as described in Equation (1). Therefore, the single intensity value $I_{x,y}$ at location x, y is represented by the sum of the contributions of all structure functions $f_{S,D,L}$ and the mean value μ. The structures used may vary in certain parameters, e.g., the Curvelet transform distinguishes several scales (S), directions (D), and locations (L). The appearance of the single structures is controlled by the corresponding Curvelet coefficients $k_{S,D,L}$. These complex numbers define the sine (real) and cosine (imaginary) contribution to the resulting structure. Their intensity, therefore, is proportional to the intensity of the structure in the decomposed image.

$$I_{x,y} = \mu + \sum_{Scale} \sum_{Direction} \sum_{Location} k_{S,D,L} \cdot f_{S,D,L} \tag{1}$$
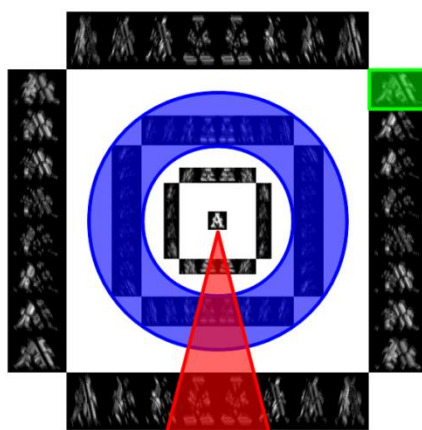
In order to illustrate the characteristics of the Curvelet decomposition, a test image (shown in Figure 1) is transformed to Curvelet coefficients whose intensity is depicted in Figure 2. In the middle, the subsampled image which corresponds to the mean μ is visible. The rings of this illustration refer to the different scales of the decomposition. Throughout all scales, slices—indicated by the red triangle—unify similar directions. For each scale, and each direction, several locations for the structures are possible that are captured by the single images. It is obvious that the main structures of the original image still

can be recognized in the coefficient images. However, each single image—indicated by the green rectangular—highlights special parts of the original image according to scale and direction.

Figure 1. Original—synthetic test image.

Figure 2. Curvelet coefficients intensity of test image—blue ring equates one scale, red triangle equates one direction, green rectangle equates the locations of one scale and one direction.

The decomposition into Curvelet coefficients cannot only be used for image analysis but also for image manipulation. Due to the direct description of structures certain structure types can be omitted or intensified, e.g., Figure 3 shows the image reconstructed by using the Curvelet coefficients of one scale (*cf.* blue ring in Figure 2) exclusively. Hence, all structures have approximately the same length. If not, they are composed out of single structures sharing the same length. Figure 4 illustrates the reconstruction of the Curvelet coefficients belonging to structures with diagonal direction (*cf.* red triangle in Figure 2). Thus, only diagonal lines are apparent. Figure 5 depicts the image reconstructed by omitting all Curvelet coefficients at the edges of the single images (*cf.* green rectangle in Figure 2). While the original image appears in the middle the intensity reduces towards the edges of the image. This proves that the range of the single functions is restricted. That is the important difference between novel image representations, such as Wavelets or Curvelets, and the well-known Fourier transform. The functions of the Fourier transform—sine and cosine—have an infinite influence, so they do not need any location information. As the influence of the Curvelet functions decreases with increasing

distance from the center depending on the scale and the direction, all three parameters—scale, direction, location—have to be defined for each function. However, similar to image processing in Fourier domain artifacts (overshoots) appear in Figures 3–5 because just a fix threshold and no window function is applied. In order to avoid these artificial structures in the reconstructed images, we introduce a special weighting function in Section 2.2. In contrast to that, instead of suppressing artificial structures the structure amplification might also be explicitly utilized for edge detection purposes [21].

Figure 3. Image reconstruction using Curvelet coefficients of one single scale.

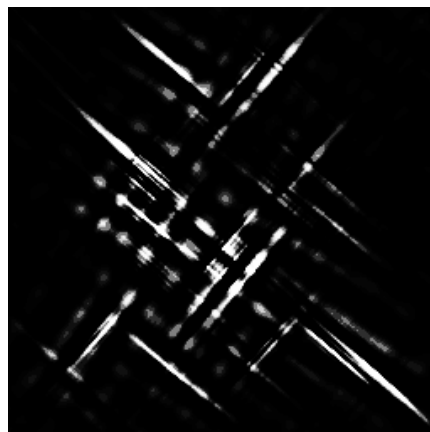**Figure 4.** Image reconstruction using Curvelet coefficients of diagonal directions.

Figure 5. Image reconstruction using Curvelet coefficients of center locations.

2.1.2. Curvelet-Based Image Comparison

Due to the multiplicative characteristics of SAR intensity images the intensity quotient in logarithmic scale is widely used in SAR remote sensing as relative change measure. It can be defined either as logarithm of the quotient or as difference of the logarithms of the single images, see Equation (2).

$$\Delta_{log}I = \log\frac{I_2}{I_1} = \log I_2 - \log I_1 \tag{2}$$

The change image—normally calculated in spatial domain, *i.e.*, pixel by pixel—is highly affected by noise. As the enhancement of this change measure is a difficult task due to the absence of distinct structures we try to reformulate the change measure in terms of Curvelet coefficients in Equation (3). Applying the Curvelet transform (T) and the inverse Curvelet transform (T^{-1}) subsequently to the single images in the definition taken from Equation (2) does not change Equation (3). The Curvelet transform T outputs the Curvelet coefficients so that the definition in Equation (1) can be inserted into Equation (3) for both images. Being a linear description, the distribution law applies and the functions can be differentiated before performing inverse transform. As only the coefficients vary—but, the function definitions are identical—for two equally sized images, the differentiation even reduces to the Curvelet coefficients exclusively, see Equation (3).

Thus, the inverse transform of the differential Curvelet coefficients directly results in the change image, *i.e.*, the logarithm of the intensity quotient. In other words, the structures apparent in the input images can be transferred to Curvelet coefficients and directly compared by differentiating the corresponding coefficients which is much more stable than searching for structures in the noisy change image.
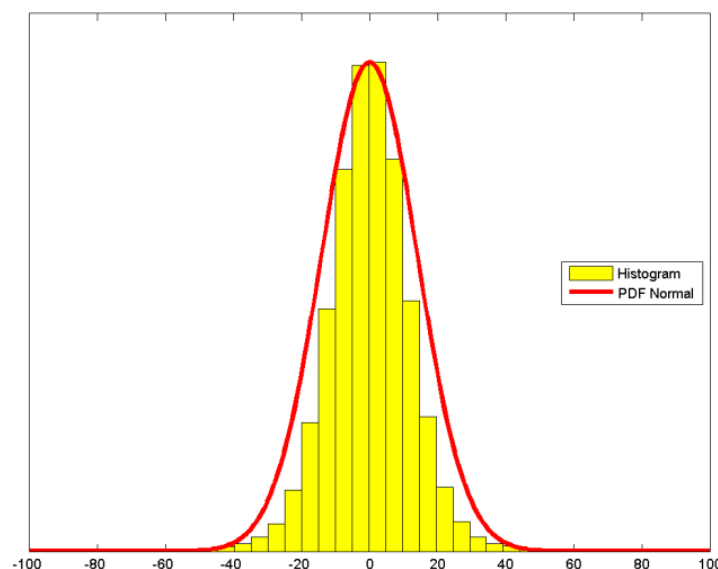
$$
\begin{aligned}
\Delta_{\log I} &= T^{-1}[T(\log I_2)] - T^{-1}[T(\log I_1)] \\
&= T^{-1}\left[\mu + \sum_S\sum_D\sum_L k_{S,D,L}\cdot f_{S,D,L}\right]_2 - T^{-1}\left[\mu + \sum_S\sum_D\sum_L k_{S,D,L}\cdot f_{S,D,L}\right]_1 \\
&= T^{-1}\left[\mu_2 - \mu_1 + \sum_S\sum_D\sum_L k_{S,D,L\,2}\cdot f_{S,D,L} - \sum_S\sum_D\sum_L k_{S,D,L\,1}\cdot f_{S,D,L}\right] \\
&= T^{-1}\left[(\mu_2 - \mu_1) + \sum_S\sum_D\sum_L \left(k_{S,D,L\,2} - k_{S,D,L\,1}\right)\cdot f_{S,D,L}\right] \\
&= T^{-1}\left[(\mu_2 - \mu_1) + \sum_S\sum_D\sum_L dk_{S,D,L}\cdot f_{S,D,L}\right]
\end{aligned}
\tag{3}
$$

2.1.3. Curvelet Coefficient Statistic

As the Curvelet representation is bijective (*i.e.*, one-to-one and onto), noise is represented as well as distinct information. But, in contrast to the spatial domain, noise can easily be separated from structures in the Curvelet coefficient domain. Strong longitudinal structures are known to have higher coefficients than weaker structures that do not exceed noise level. In order to find the border between noise and real structure information the distribution of the Curvelet coefficients, *i.e.*, the real and imaginary parts, is studied in the following, see Figures 6 and 7.

Obviously, the real and imaginary parts of the Curvelet coefficients follow more or less a normal distribution with its mean in zero and a similar standard deviation. This was expected because of two facts: At first, the large number of real random values associated with the Curvelet coefficients real and imaginary parts induces compulsorily a normal distribution because—according to the central limit theorem [22]—any distribution tends towards a normal distribution for a sufficiently large number of samples. And secondly, regarding change images in remote sensing applications—where (without exception) only local changes are present—the most part of the image is more or less stochastic, *i.e.*, there are only few distinct structures that possibly affect the normal distribution of the coefficients. Above all, the single sub-band coefficients being normalized during Curvelet transform [23] make a special treatment of the sub-bands dispensable. Thus, if the image contents were completely stochastic, the random combination of real and imaginary parts would result in amplitudes that follow a Rayleigh distribution—similar to SAR amplitudes of distributed targets as reported in [24]—uniformly over all sub-bands. The sole parameter of the Rayleigh distribution function then is equal to the standard deviation of the real and imaginary parts. Figure 8 illustrates the analytical probability density function (PDF), the cumulative density function (CDF), and the empirical histogram of the Curvelet coefficient amplitudes. Indeed the histogram of the coefficient amplitudes does not deviate that much from the Rayleigh PDF except for very low and very high values. On the one hand, there are more low values in the empirical histogram than expected. On the other hand, there are more high amplitudes than the Rayleigh PDF would predict. From this, it follows that the combination of real and imaginary parts is not completely stochastic, but partly deterministic which is caused by the small amount of distinct structures in the change images.

Figure 6. Histogram of the real parts and normal probability density function.

If we assume again a purely stochastic image content the Rayleigh distribution would describe the histogram of the coefficient amplitudes. Thus, the Rayleigh CDF would fit the quantiles of the coefficient distribution. For example, removing the 99.9% quantile of the Rayleigh distribution means that only 1‰ of the coefficients remain, in other words the noise content of the image is reduced to 1‰ of its initial value. Keeping in mind that there are some distinct structures in the image, *i.e.*, not

only noise, the noise content is reduced to a ratio far below 1‰. One might say the noise contribution is completely removed. In practice, this border turned out to be very effective for general image enhancement purposes [19].

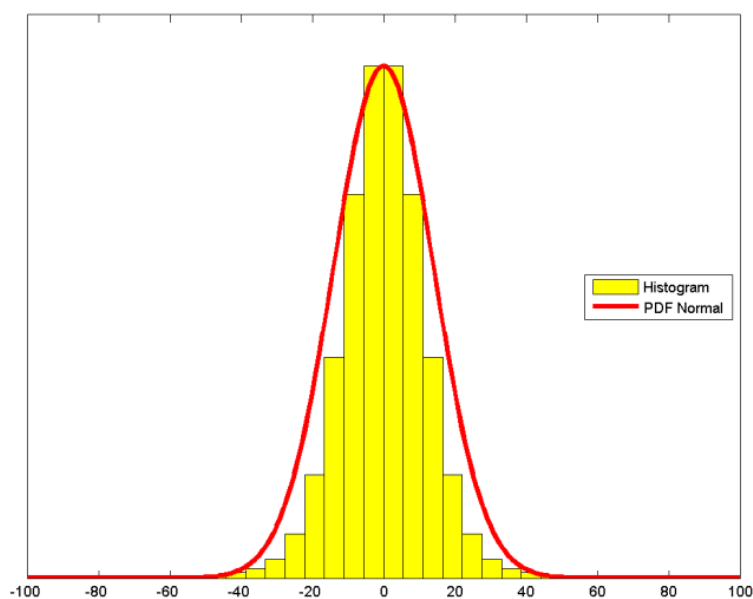**Figure 7.** Histogram of the imaginary parts and normal probability density function.
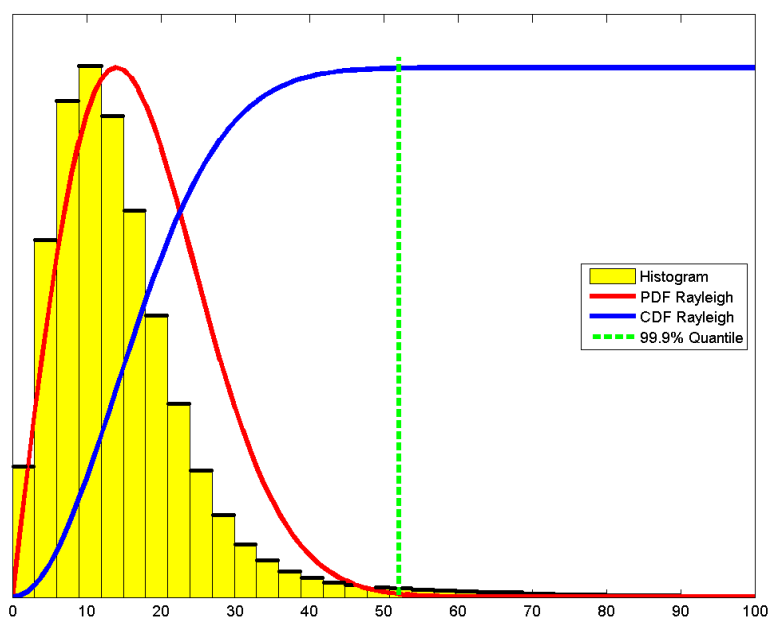

Figure 8. Histogram of the coefficient amplitudes and Rayleigh probability density (red) and cumulative density function (blue) with 99.9% quantile (green).

2.2. Curvelet-Based Image Enhancement

The preceding subsection studied the use of Curvelets for image comparison and how distinct structures might be distinguished from noise. Unfortunately, simple thresholding as derived above and often discussed in literature [25,26] produces artifacts due to the sharp decision between coefficients that are kept unchanged and those that are completely removed. Nevertheless, simple or adaptive

thresholding still is state of the art in Curvelet-based image denoising [27]. One can refer this behavior to the image processing in the frequency domain. When certain frequencies are removed from the entity without applying special window functions, overshoots are produced in general [28]. The effect is similar to removing certain stationary waves in the Curvelet coefficient domain. If no window function is defined, the overshoots express in ridge-like artifacts because of the Ridgelet used as basic element of the Curvelet transform [17]. Therefore, this section will develop a special window function for Curvelet coefficients—referred to as weighting function in the following—that guarantees a smooth ascent from suppressed to preserved coefficients and, thus, avoids artifacts in the resulting change image at the best.

2.2.1. Definition of the Weighting Function

The requested weighting function G given in Equation (4) is expected to be continuous as the Curvelet coefficients can adopt any arbitrary float value. For the sake of convenience, it should be applied to the differential Curvelet coefficients only before the change image is transformed back to the spatial domain.

$$\Delta_{log}I = T^{-1}\left[(\mu_2 - \mu_1) + \sum_S \sum_D \sum_L G(dk_{S,D,L}, a, b) \cdot f_{S,D,L}\right] \qquad (4)$$

The difference of the mean values $\mu_2 - \mu_1$ is assumed to be noise-free because of the very high number of incorporated measurements. Furthermore, as mainly local changes are encountered the mean differences always range near zero. The coefficients are weighted in relation to their amplitude solely. Other characteristics, such as scale, direction, location, or the complex phase angle are not considered because no single scale, direction or location should be preferred to others. As the information content varies with the number and the strength of changes, the weighting function is adapted to each change image separately via the corresponding coefficient distribution, see preceding subsection.
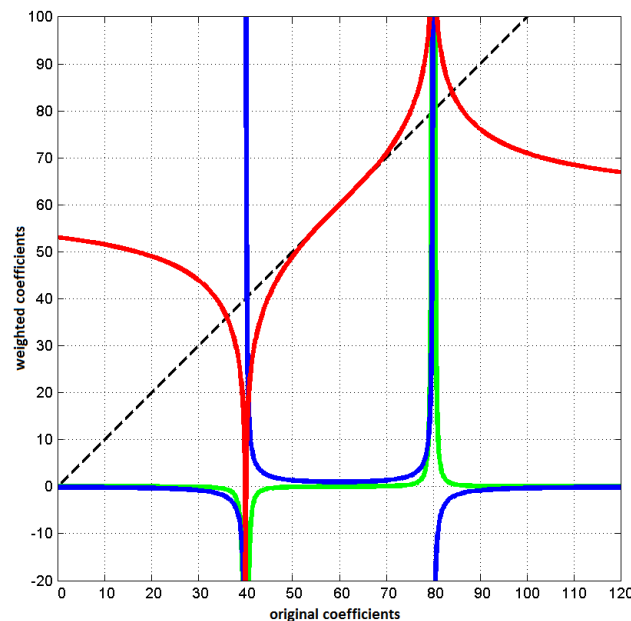
2.2.2. Detailed Characteristics of the Weighting Function

Out of the coefficient statistics the two values a, b are calculated that represent the lower border a—all coefficients below that border are completely removed because being addicted to noise—and the upper border b, respectively—all coefficients exceeding this border are seen as distinct structural information and thus, kept unchanged. In-between the monotonically increasing weighting function applies. At the borders of the weighted range the function of the weighted coefficients has to meet special requirements that are summarized in Equation (5).

$$G(a, a, b) = 0 \qquad\qquad G'(a, a, b) = \infty$$
$$\qquad\qquad\qquad\qquad\qquad\qquad\qquad\qquad\qquad\qquad\qquad\qquad (5)$$
$$G(b, a, b) = b \qquad\qquad G'(b, a, b) = 1 \qquad\qquad G''(b, a, b) = 0$$

At the lower border—symbolized by a—the weighted coefficients are set to zero, *i.e.*, their influence is completely removed. The gradient must be positive. Its absolute value is not defined exactly. Ideally, the weighting function adapts to a vertical straight line, *i.e.*, with an infinite positive gradient. At the upper border b the value function should reach the bisectrix so that the strength of the

coefficients in b and above remains unchanged. Additionally, the gradient should reduce to one, and the curvature should reach zero in order to remain continuous—with respect to the bisectrix—even in the second derivative. Thus, artifacts caused by widely-used discrete or discontinuous weighting functions—like simple thresholding—can be avoided. Any function complying with these prerequisites thus can act as window function for image enhancement based on Curvelet coefficients.

Figure 9. Modified Area Hyperbolic Tangent function (red), gradient (blue) and curvature (green) for $a = 40$ and $b = 60$.

2.2.3. The Modified Inverse Hyperbolic Tangent Function as Weighting Function

Although there are several ways how to design an equivalent weighting function, only one function—the modified area hyperbolic tangent—will be presented in the following (Equation (6)) without loss of generality because it perfectly fits in the hyperbolic tangent environment established for SAR imagery in [19]. It should be mentioned here that the choice of the weighting function has a negligible impact on the results as long as the requirements above are met, *cf.* Equation (5).
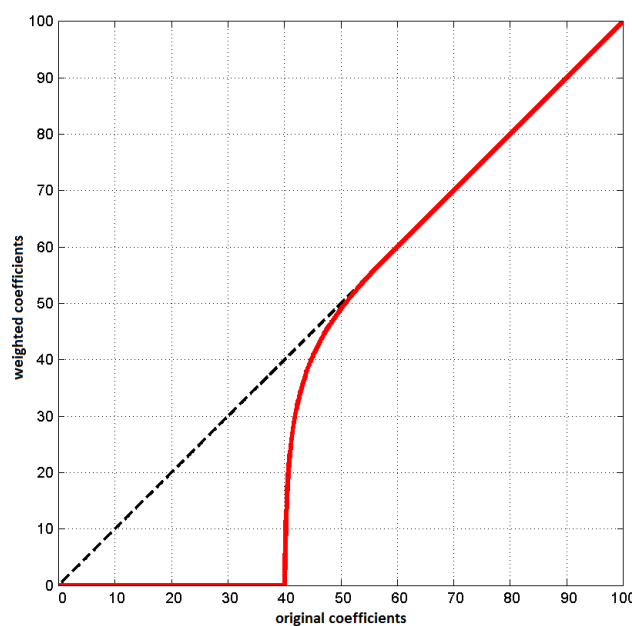
$$G\big(\big|dk_{S,D,L}\big|, a, b\big) = \frac{a}{2} \cdot \ln \frac{a + \big(\big|dk_{S,D,L}\big| - b\big)}{a - \big(\big|dk_{S,D,L}\big| - b\big)} + b \tag{6}$$

In order to prove the suitability, Figure 9 draws the weighting function as well as the first two derivatives. The function crosses zero near the lower border ($a = 40$). Although the exact position of the intersection with the abscissa slightly is above the lower border—because its vertical asymptote is located in a—the minimal deviation can be neglected. Its gradient indicates that it is vertically ascending. In-between the two borders a, b the function is monotonically increasing while the gradient reduces towards one and the curvature increases towards zero. At the upper border ($b = 60$) all requirements are perfectly fulfilled.

Therefore, the modified area hyperbolic tangent function is appropriate for weighting the Curvelet coefficients in-between two borders possibly determined by the coefficient statistics, see Figure 10.

Below the null, near the lower border (here located in 40) all coefficients are set to zero. Above the upper border (here defined as 60) all coefficients remain unchanged. These borders are variable and can be replaced by statistically derived values. In practice the 99% quantile as lower border and the 99.9% quantile as upper border proved to deliver satisfying results. In other words, only 1‰ of the coefficients are preserved, while 9‰ (between 99.0% and 99.9%) are weighted by G and 99% are completely removed. This is equivalent to an image compression to 1% of its original size. Due to the special characteristics of Curvelets regarding longitudinal structures in the image [17], this small portion shows up to suffice an adequate image reconstruction. Finally, being adapted to the image content via the variance of the Curvelet coefficients real and imaginary parts, these borders are valid for all kinds of applications [19].

Figure 10. Weighted coefficients (red) for the borders $a = 40$ and $b = 60$ in relation to the bisectrix.

3. Validation

This chapter investigates the reliability of our new Curvelet-based change detection approach. The validation of SAR change detection results in general is a very challenging task. Regardless of the field of application any measurements should be validated with respect to a method that is known to be more accurate in the order of at least one magnitude. In the case of space-borne SAR sensors only SAR systems at the same wavelength, but with a much higher geometric resolution and a lower noise floor could deliver comparable results, e.g., air-borne SAR sensors. Unfortunately, because of the much lower altitude the incidence angle range is wider with air-borne sensors and it is well-known that the incidence angle has an important impact on the measurement that can only be corrected for isotropic and non-dispersive targets. Thus, even for an air-borne reference acquired simultaneously from the same looking direction systematic deviations cannot be eliminated. Although taking into account other data sources like optical images or *in situ* data would promise highly accurate information the validation would always compare the different acquisition techniques as well, e.g., optical *versus*

radar. As we aim at validating the Curvelet-based approach against other image interpretation techniques we decided in favor of a reference produced by experienced human SAR interpreters. Additionally, two common automated techniques, the simple log-ratio and the log-ratio of GMAP filtered original images are mentioned as well. For the sake of convenience one 512 ×512 pixel subset of the HH amplitude of two high resolution spotlight enhanced ellipsoid corrected products acquired by TerraSAR-X over the industrial harbor of Mannheim (Germany) on 21 September 2008, and 2 October 2008, respectively (© DLR 2008) is chosen as input though the processing of the whole scene would also be possible. Both workflows—of the automated and of the manual procedure—are explained in the following. The results of the comparison conclude this chapter.

3.1. Automated Change Detection

The workflow of the automated approach is given in Figure 11. The procedure starts with the overlapping parts of two geocoded images (*cf.* [29]). Thanks to the high quality of the orbit data, no further co-registration step is necessary for amplitude based change detection as reported in [30]. The logarithmic intensities of these subsets are transformed into Curvelet coefficients and differentiated in order to generate the change image. The differential coefficients are subsequently weighted by the modified area hyperbolic tangent function derived above with the lower border at 1% and the upper border at 1‰, *i.e.*, in theory 99% of the coefficient are completely removed and only 1‰ of the coefficients remain unchanged, while all coefficients in-between (from 99.0% to 99.9%) are weighted continuously. Afterwards the change image is transformed back from the coefficient to the spatial domain. Both transformations are performed by MATLAB implementations available at [31] automatically selecting the appropriate number of subbands, rotations, and locations for the optimal image description with respect to the image dimensions. In the case of the standard techniques the change image is directly generated as log-ratio of the input images with or without additional speckle suppression.

Figure 12 displays a color composition of the original amplitude images that will be used for manual classification later on. This test site is deliberately chosen because of the presence of numerous deterministic scatterers that move in-between the two acquisitions which simplifies the manual change detection by operators. Human interpreters still providing the most reliable reference we decided to choose this relatively simple scenario. In order to compare our new approach to standard techniques the pixel-based log-ratios of the radiometrically enhanced TerraSAR-X images [32] incorporating approximately five looks with and without supplementary speckle suppression using the GMAP filter [33] are considered as well, see Figures 13 and 14. The results of our automated change detection approach—performed in 15 seconds by a MATLAB implementation on a SPARC-SOLARIS server—are shown in Figure 15. Obviously only few distinct structural changes remain after coefficient weighting. Small-scale changes mainly caused by noise are completely removed while the standard techniques (Figures 13 and 14) still deliver numerous small change patterns mainly on open water surfaces. The continuous change image is classified as follows: less than −10 dB equals negative change (in blue), more than +10 dB equals positive change (in red), otherwise no change detected (transparent). The high threshold of 10 dB—corresponding to an increase to ten times or a decrease to the tenth of the original value—is adequate because it is hard for human interpreters to recognize lower changes on the

one hand. And on the other hand, as the scene covers mostly changes on deterministic targets, it is far sufficient, *i.e.*, lower more sensitive thresholds are not necessary.

Figure 11. Flow chart of the Curvelet-based change detection.
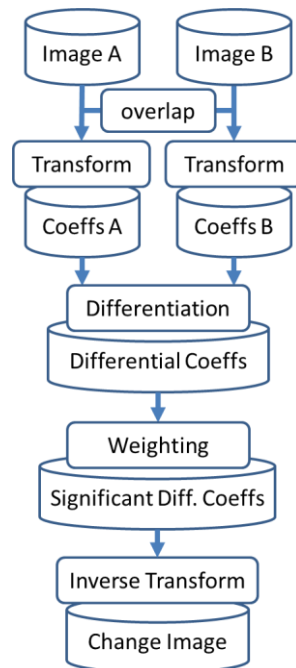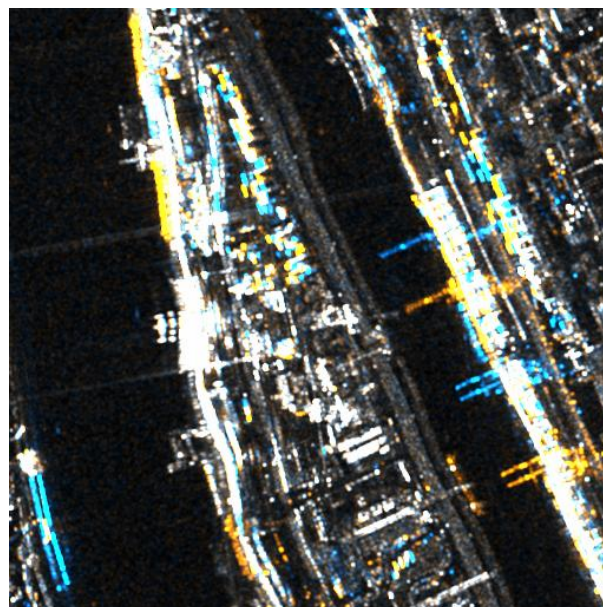

Figure 12. Color composition of both amplitude images, positive changes appear in orange, negative changes appear in blue.

3.2. Manually-Derived Reference

The combined image in Figure 12 is given to five SAR experts who are asked to mark positive as well as negative changes. According to the color composition positive changes appear in orange and negative changes in blue while gray tones indicate similar backscattering values for both acquisitions.

If the images were compared visually using neither overlaying nor color coding, no difference could be recognized. The time needed for the classification was about 15 min. As the five manually-derived results are not identical, the mode (majority) was chosen as reference, *i.e.*, if three or more interpreters agree that a pixel has changed in a certain direction, this change is accepted, see Figure 16. Obviously the class "stable" (*i.e.*, no change) dominates as expected. Increases and decreases in the amplitude data appear nearly equally frequent.

Figure 13. Automatically detected changes over 10 dB using pixel-based log-ratio with the amplitude image in the background.
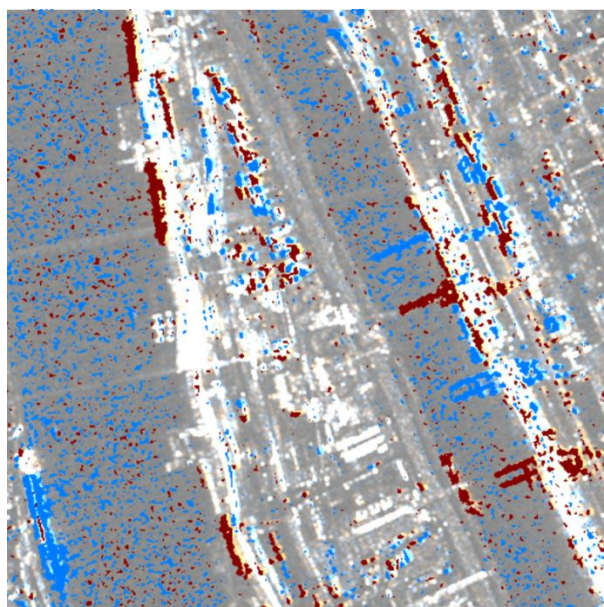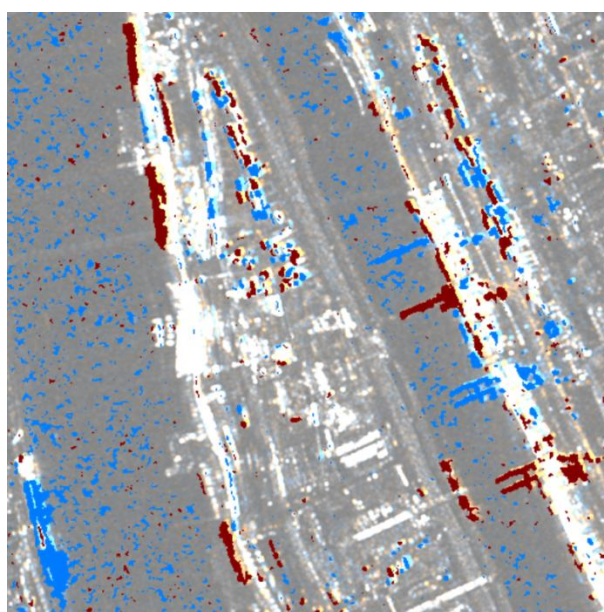

Figure 14. Automatically detected changes over 10 dB using pixel-based log-ratio after GMAP filtering with amplitude image in the background.

In order to estimate the reliability of the reference data, the accordance of the five interpreters is evaluated per class in Table 1. The class "stable" was congruently classified by all five interpreters in

more than 90% of the samples in the reference image. Due to the numerous occurrence of that class the high concordance is not surprising. When looking at the other classes the values for three to five identical classifications range between 20% and 40%. Further tests report even lower values for the same scenario [19]. As the concordance in classifying changes is surprisingly low, the location of the discrepancies is checked in Figure 17. The colors in the image refer to the colors used in Table 1.

Figure 15. Automatically detected changes in the HH amplitude over 10 dB using our Curvelet-based method with the amplitude image in the background.
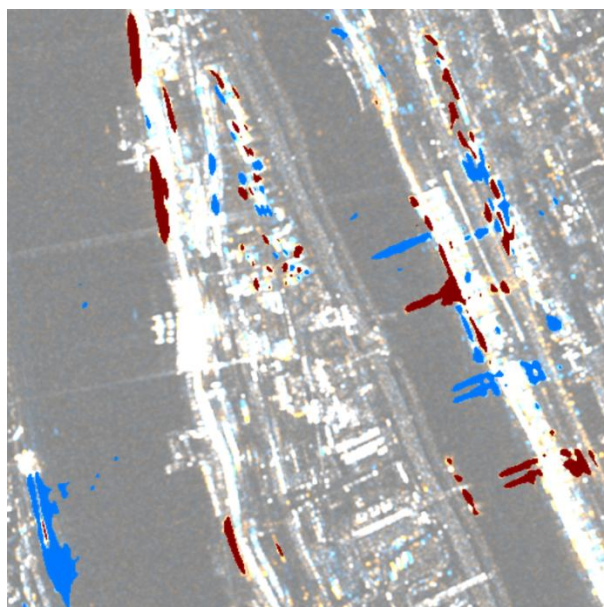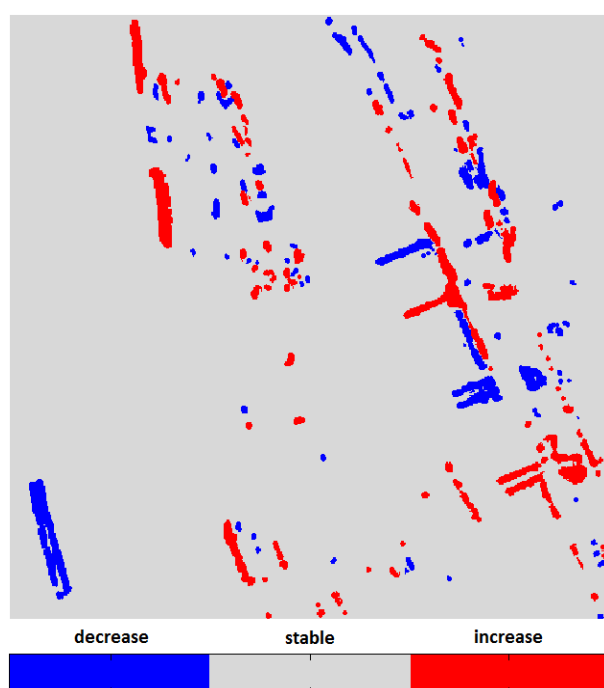

Figure 16. Mode of the five manually derived references for the change in amplitude.

Obviously the high discrepancy can be referred—in most cases—to the size of the observed changes. That means that the interpreters used finer or coarser tools to mark the changes. Additionally,

some small-sized changes have not been detected by all interpreters. In this example all larger changes were found by all human interpreters. According to [19] even obvious changes are sometimes missed by human interpreters. As automated approaches in general do not use semantic information, they indicate each deviation in the backscattering independent of its location or environment. In contrast to that, human interpreters pre-classify the image in interesting parts, e.g., the harbor, and regions of no interest, e.g., open water. Thus, they save time because the area to be process significantly reduces. Apart from that, distinct changes lying inside or across regions of no interest are sometimes completely missed, *cf.* [19]. In summary, even human interpreters are not able to deliver an optimal reference for the validation of the automated change detection approach, but they are still most reliable in contrast to other automated methods, which will become obvious in the next subsection.

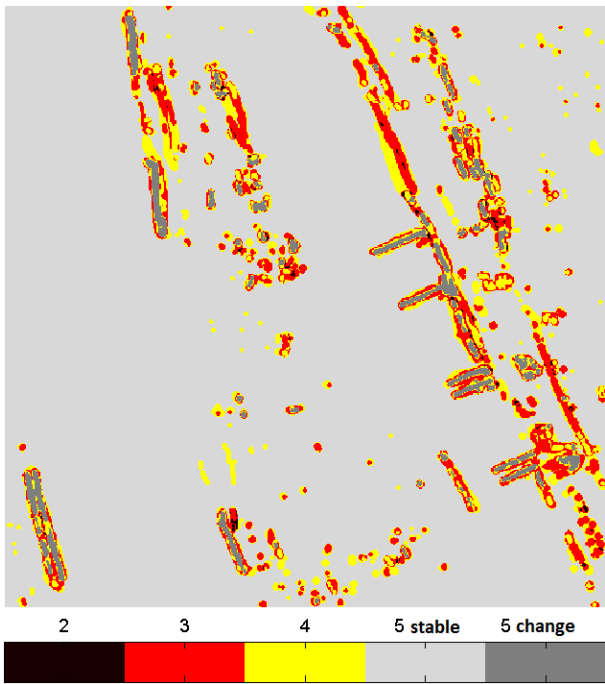**Figure 17.** Accordance amongst the five human interpreters for the change in amplitude.

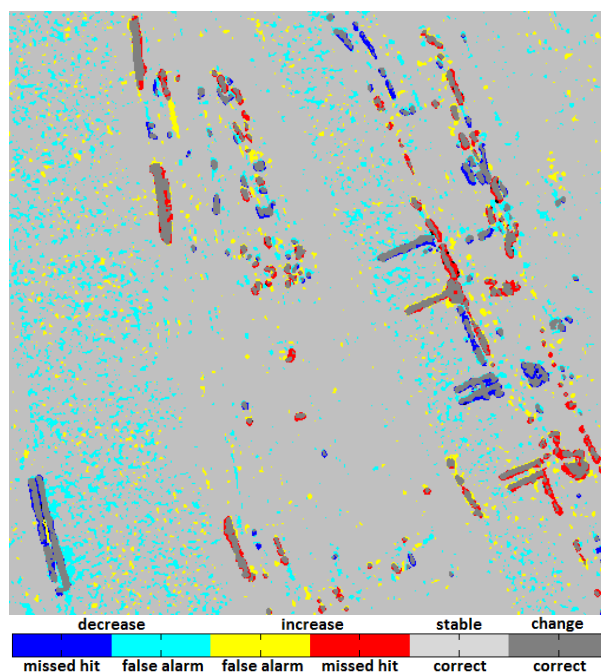**Table 1.** Concordance per class in (%) of the five human interpreters.

HH Amplitude		Accordance per Class		
		3	**4**	**5**
	decrease	35.17	27.04	37.80
mode	stable	3.34	5.03	91.62
	increase	35.73	29.78	34.49

3.3. Accuracy Assessment

In the following, the changes marked by the human interpreters are compared to changes over 10 dB produced by the pixel-based log-ratios with and without supplementary GMAP speckle suppression—referred to as standard techniques—as well as by the novel Curvelet-based change detection. The confusion matrix is generated pixel-by-pixel although an object-based accuracy assessment would promise better results. However, as there are no standards for the choice of

parameters (object size, buffer size, overlay ratio, *etc.*) the results could be manipulated arbitrarily. The listed values are normalized by the total number of pixels and output as percentage. The color of the boxes is equal to the color used to illustrate the corresponding locations in Figures 18–20. Gray tones mark correctly classified pixels. Blue and turquois indicate missed hits and false alarms respectively of negative changes while red and yellow refer to missed hits and false alarms of positive changes.

Figure 18. Location of the confusion matrix elements for the change in amplitude using pixel-based log-ratio.

The confusion matrix for the simplest method, *i.e.*, the pixel-based log-ratio on radiometrically enhanced TerraSAR-X amplitude images, is given in the upper part of Table 2. The surprisingly high total accuracy can be referred to the numerous occurrence of the class "stable" covering nearly 95% of the image. The completeness—related to missed hits—is quite good ranging around 70%. Considering Figure 18 which shows the location of the missed hits reveals that they usually surround larger change patterns, *i.e.*, the missed hits are caused by a different estimation of the size of the change. The correctness—associated with the false alarm rate—is very low reaching 22% for false alarms of negative changes. These are almost exclusively small-scale changes on the open water surface presumably caused by noise, see Figure 18. As water in general causes a very weak backscattering signal, even slight changes can provoke high change rates in the log-ratio. Those noise-induced hits have to be removed by an adequate filtering.

Therefore, the input images have been pre-processed by the GMAP filtering method (using ERDAS IMAGINE® 2011, window size: 7, coefficient of variation: 0.2). The confusion matrix in the middle of Table 2 proves that there is a significant increase in the total accuracy to more than 95%. Although the completeness slightly decreases, the missed hits mass around larger change patterns (Figure 19) and thus, can be attributed to the different size of the changes: these detected by the automated approach and those marked by the human interpreters. In contrary to that, the correctness improves to 47% for negative changes and even to 70% for positive changes. Looking at Figure 19, there are still

too many false alarms on the river as well as in the upper right corner of the image. In order to achieve reliable results, those false alarms need to be removed.

Figure 19. Location of the confusion matrix elements for the change in amplitude using pixel-based log-ratio with preceding GMAP speckle suppression.
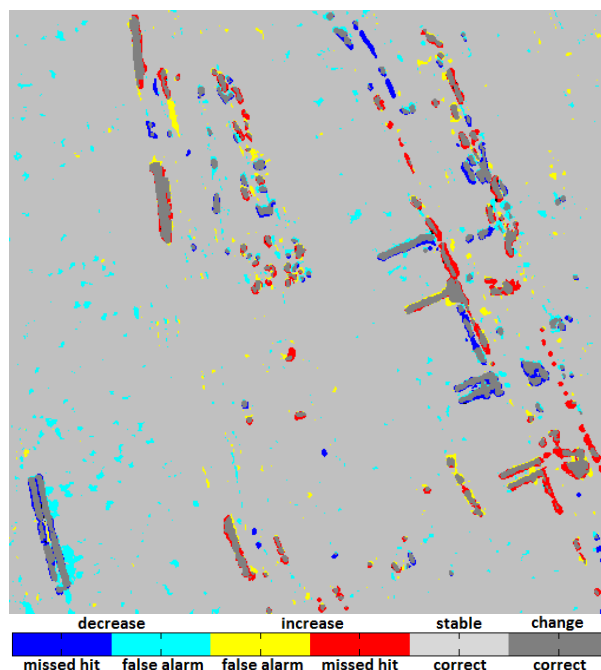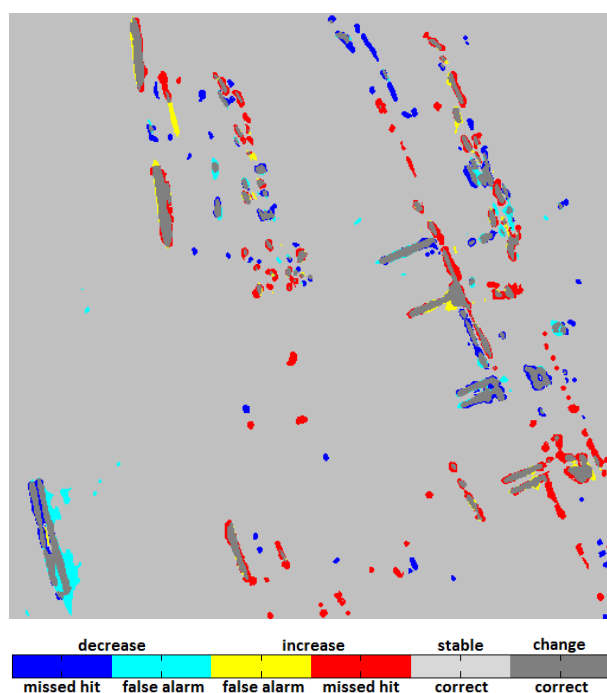

Table 2. Confusion matrix for all three automated methods in comparison to the manual reference

HH Amplitude		Manual Reference				
		Decrease	*Stable*	*Increase*	Σ	Correctness
Log-Ratio	*Decrease*	1.61	5.65	0.02	7.28	**22.11**
	Stable	0.61	86.51	1.05	88.16	**98.12**
	Increase	0.01	2.42	2.12	4.55	**46.62**
	Σ	2.23	94.58	3.19	100.00	
	Completeness	**72.20**	**91.46**	**66.54**	**Total Accuracy 90.24**	
		Decrease	*Stable*	*Increase*	Σ	Correctness
Log-Ratio after GMap Filtering	*Decrease*	1.55	1.72	0.01	3.29	**47.18**
	Stable	0.67	91.99	1.15	93.82	**98.06**
	Increase	0.01	0.87	2.03	2.90	**69.97**
	Σ	2.23	94.58	3.19	100.00	
	Completeness	**69.52**	**97.26**	**63.57**	**Total Accuracy 95.57**	
		Decrease	*Stable*	*Increase*	Σ	Correctness
Curvelet Approach	*Decrease*	1.32	0.52	0	1.85	**71.61**
	Stable	0.91	93.80	1.60	96.31	**97.39**
	Increase	0	0.25	1.59	1.84	**86.26**
	Σ	2.23	94.58	3.19	100.00	
	Completeness	**59.37**	**99.18**	**49.70**	**Total Accuracy 96.71**	

Finally, the changes detected by the Curvelet-based approach are compared to the manually-derived changes see the bottom of Table 2. Apparently, there is no confusion between positive and negative changes *i.e.*, the direction of the changes always is correctly determined in contrast to the standard techniques above. The total accuracy now almost reaches 97%. The correctness once again raises and ranges around 72% for negative changes and even 86% for positive changes, *i.e.*, the Curvelet-based technique is robust and the automatically detected changes are quite reliable. The completeness again is lower ranging around 54%, *i.e.*, the reference is indicating more changed pixels than the automated approach produces. It was stated before that some of the interpreters used quite coarse tools to mark the changes. Therefore, the changes in the reference might be wider than the changes measured by the automated approach. Due to the pixels at the edges captured by the reference, but not captured by the automated approach the completeness values drop down. The confused pixels (see Figure 20)—mainly the missed hits—are all restricted to the edges of detected objects. Apart from that, some false alarms are visible in the harbor area. Those are small objects that have not been identified by the human interpreters. However, it is reasonable that these are real changes, e.g., the neighbored blue and red points in the middle of Figure 20 certainly refer to vehicles that have been moved from the blue positions the red positions in-between the two image acquisitions. Finally, it has to be mentioned that the very high accuracy stated in Table 2 relativizes keeping in mind the quite low concordance of the visual interpreters who produced the reference data set. Apart from that, the visual interpretation still provides the most reliable even though most expensive image interpretation technique.

Figure 20. Location of the confusion matrix elements for the change in amplitude using our Curvelet-based method.
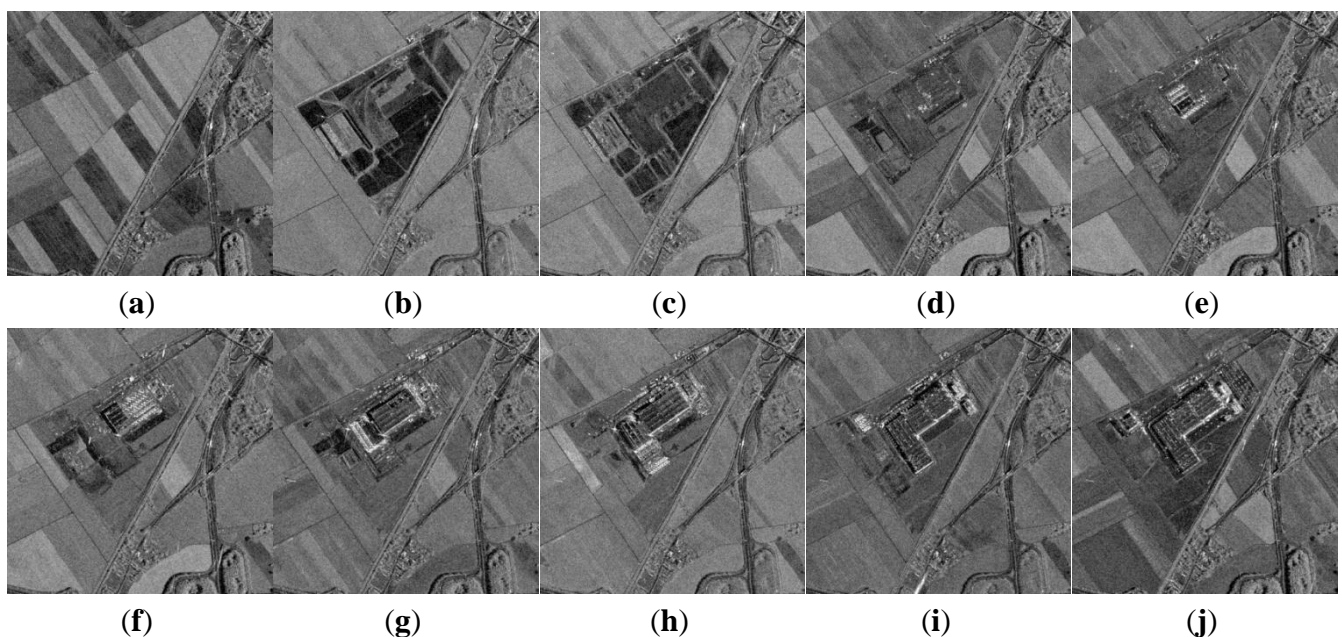

We can conclude that all changed objects that have been identified by the human interpreters have been detected by the automated approaches as well. Significant deviations can be observed only in the size of the objects. In comparison to the human interpreters the automated approaches deliver much

faster and in general more complete results. But, the reliability of the indicated changes is highly variable. None of the standard techniques tested here could compete with our Curvelet-based approach in reducing the false alarm rate and, thus, guaranteeing reliable results. In contrast to the visual interpretation, the automated methods are repeatable: Even if the same image was given to same human interpreter several times, each product will be different from the others [19]. However, human interpreters are able to pre-classify the image and then distinguish between changes of interest (e.g., changes on industrial facilities) and changes of no interest (e.g., changes on water surfaces caused by varying wind conditions). For automated approaches, this "masking" of areas of interest has to be done in a further step using additional geo-information on the land cover in the observed scene.

4. Application

Now that the suitability of the novel Curvelet-based change detection approach is proven, the method can be applied to longer time series. In the following, the multi-temporal images are shortly presented, as well as the changes detected by the Curvelet-based approach. The last section of this chapter explains how these results can easily be utilized for construction site monitoring.

Figure 21. Subset of TerraSAR-X high resolution spotlight time series over Ludwigshafen acquired during several overflights between May 2008 and July 2010: (**a**) 9 May 2008. (**b**) 4 December 2008. (**c**) 13 March 2009. (**d**) 23 July 2009. (**e**) 25 August 2009. (**f**) 16 September 2009. (**g**) 30 October 2009. (**h**) 21 November 2009. (**i**) 2 April 2010. (**j**) 21 July 2010.
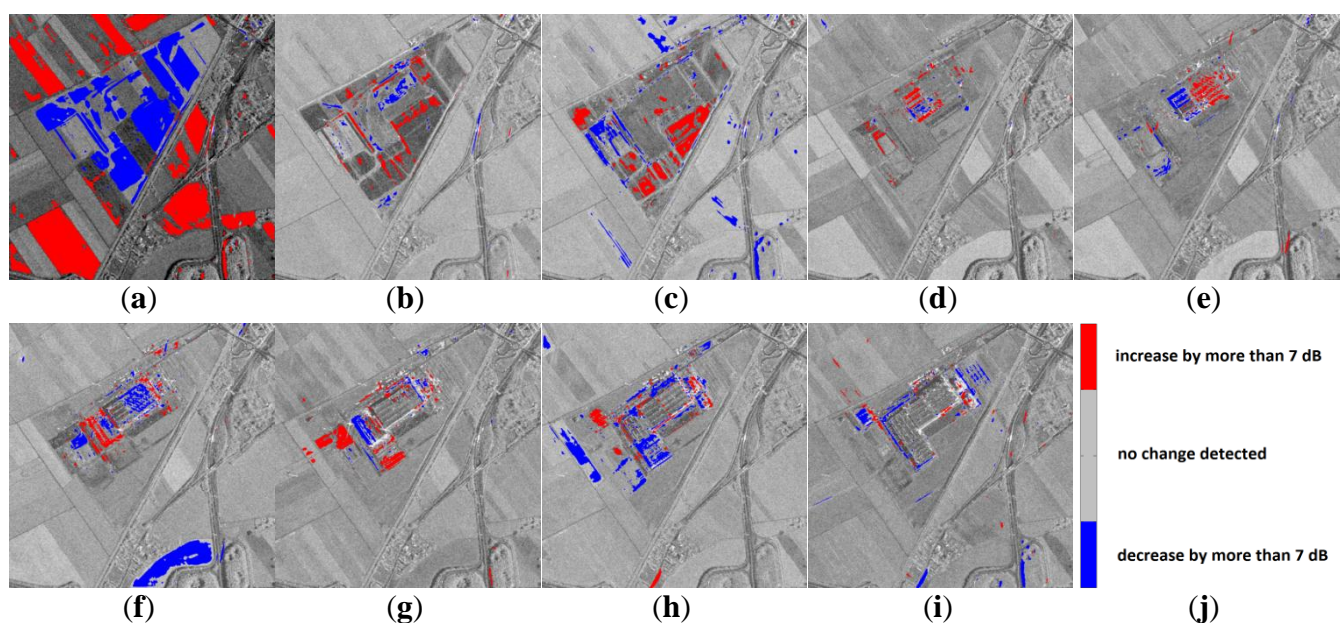

4.1. Image Sequence

The construction of a new factory hall on former agricultural land near Ludwigshafen in southern Germany was observed using high resolution spotlight acquisitions of TerraSAR-X. The images are ordered in the enhanced ellipsoid corrected product type with radiometric enhancement, *i.e.*, they share

a nominal look factor of about 7.6 and a corresponding pixel spacing of 1.25 m. Due to the high accuracy of the science orbit data—less than one decimeter—no further co-registration is necessary. As the first images are already acquired, long before the start of the construction, and also during winter time—where no construction activities take place—only ten images out of the dense time series are chosen that represent the main steps in the construction progress, see Figure 21. The first image still displays the former rural landscape on 9 May 2008, before the construction works begin. In the second image from 4 December 2008, earthwork already started. Arising brighter points indicate new parts of the future building in the following images taken on 13 March 2009, 23 July 2009, 25 August 2009, 16 September 2009, 30 October 2009, 21 November 2009, and 2 April 2010. The last image depicts the final building complex on 21 July 2010. Fortunately, the constructor documented the construction progress in his internet presence [34] in a very detailed manner so that we can easily check the reliability of our observations.
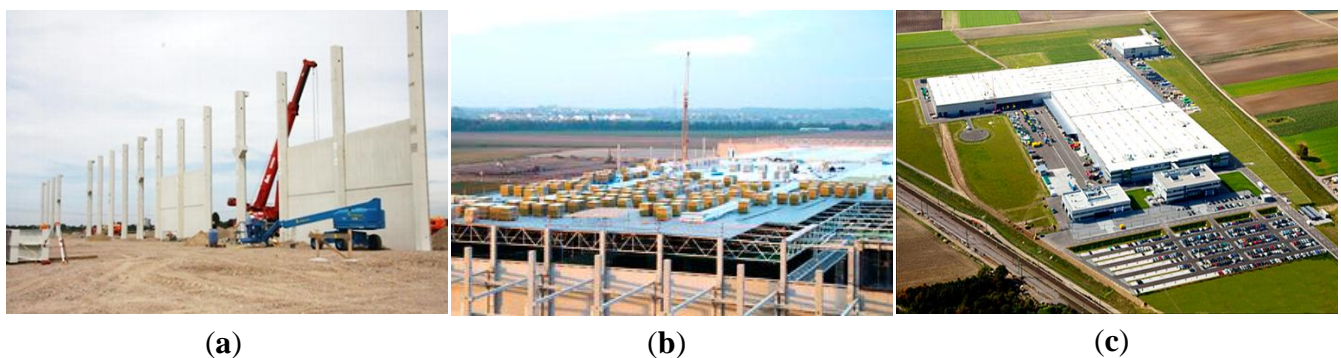
4.2. Detected Changes

The changes detected by the Curvelet-based change detection algorithm have been classified by simple thresholding into three classes: positive changes of more than 7 dB (displayed in red), negative changes of more than 7 dB (displayed in blue), and minor changes below 7 dB (transparent). The background is filled with the preceding amplitude image, see Figure 22.

Figure 22. Changes over 7 dB between neighbored image acquisitions detected in the TerraSAR-X time series over Ludwigshafen by the automated Curvelet-based approach: (**a**) 9 May 2008–4 December 2008. (**b**) 4 December 2008–13 March 2009. (**c**) 13 March 2009–23 July 2009. (**d**) 23 July 2009–25 August 2009. (**e**) 25 August 2009–16 September 2009. (**f**) 16 September 2009–30 October 2009. (**g**) 30 October 2009–21 November 2009. (**h**) 21 November 2009–2 April 2010. (**i**) 2 April 2010–04 December 2008. (**j**) color map.

The first change detection image Figure 22a mainly consists of large-scale changes on the future construction site and on the surrounding agricultural fields as well. However, in contrast to the fields a negative change is observed due to beginning earth moving activities. The following two time steps (b) and (c) indicate the progress in earthworks. Additionally, several small-scale changes along the road are visible which can be referred to traffic. Due to the shift of moving objects in SAR these changes often lay beside the road [35]. Change image (d) shows parallel dotted lines in the middle of the image in red, *i.e.*, these are new objects. The same objects appear in blue, *i.e.*, they disappear, in the next step (e), but new dotted lines in red are added. The same behavior can be observed for the following two steps (f) and (g): new objects appear and disappear again in the next time step.

Figure 23. Terrestrial and aerial photos of the factory hall during construction and after completion published by the factory owner in his internet presence [34]. (**a**) Erecting columns. (**b**) Roof installation. (**c**) Completed factory complex.

(**a**)   (**b**)   (**c**)

Considering just two images out of the wide choice available online (see Figure 23a,b) directly explains this behavior: Vertical structures are erected in a regular pattern which causes the parallel dotted lines of increasing intensity, see Figure 23a. In the next step the roof is installed (Figure 23b) and thus, the vertical structures are hidden which causes a decrease in backscattering exactly where the increase was detected in the preceding time step. It is remarkable that in the last two time steps (h) and (i) the building itself shows stable backscattering although it is surrounded by many small-sized changes. This indicates that the main hall already was completed at that time. The remaining works only concern the periphery, mainly the infrastructure, *i.e.*, roads, parking lots, street lamps, *etc.* The owners documentation in [34] confirms that observation.

4.3. Construction Progress Monitoring

Analyzing the difference between two images is quite useful when changes caused by a sudden event shall be mapped, e.g., in the case of natural disasters like earthquakes or floods. The comparison of the pre-event image with the post-event image directly leads to the changes in the landscape. For monitoring purposes over longer periods of time, the large number of output images has to be further reduced for clarity reasons. The optimal solution would be the joint depiction of all changes in one single output image or diagram. As in the case of construction site monitoring mainly new objects are of interest, all positive changes of more than 7 dB over the whole period of time are summed up and color coded according to their first appearance in Figures 24 and 25. The results of the pixel-based

image processing are illustrated in Figure 24. All changes extracted by the Curvelet-based approach are summed-up in Figure 25. No manual interaction was performed to produce this diagram. Obviously, the standard techniques require much post-processing effort while the Curvelet-based approach automatically detects the main structural changes and suppresses noise almost completely.

Figure 24. New objects colored according to their time of installation for the factory hall constructed near Ludwigshafen (Germany)—log-ratio thresholding.
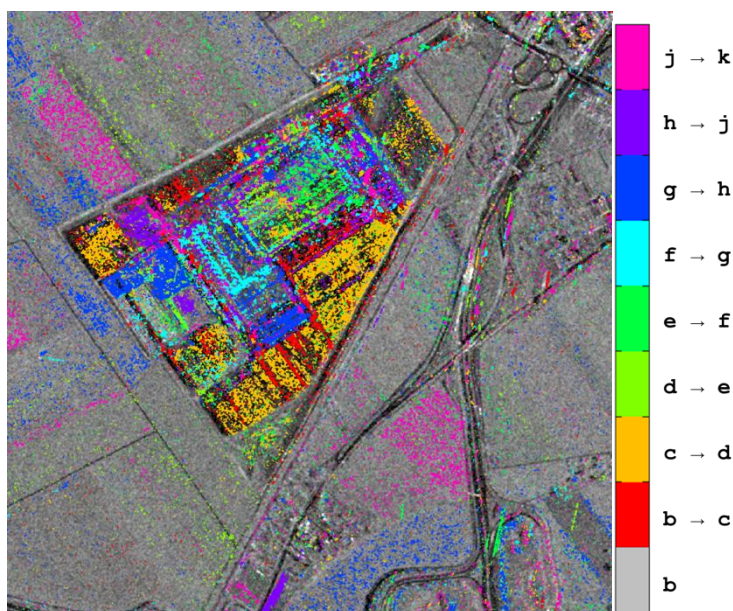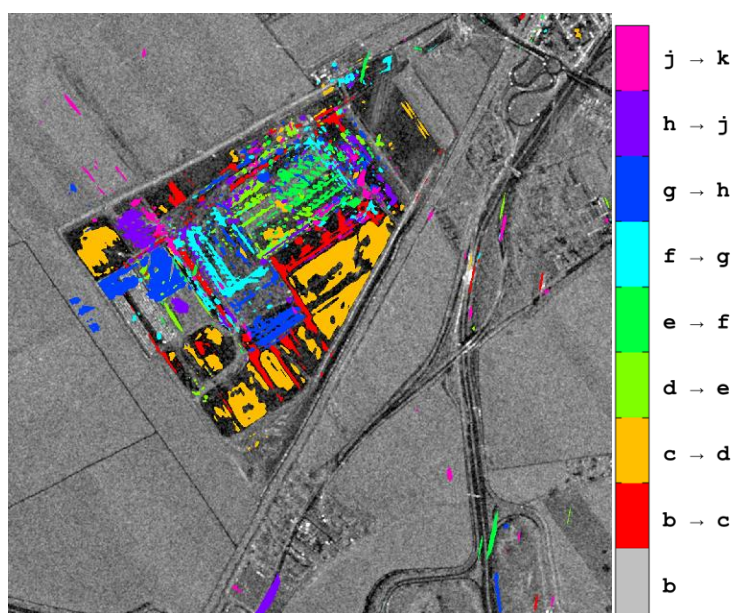

Figure 25. New objects colored according to their time of installation for the factory hall constructed near Ludwigshafen (Germany)—Curvelet-based approach.

The colors red and orange in Figure 25 indicate earthworks right at the beginning of the construction process. Green and turquois mark the main factory hall. During the time colored in blue additional building parts, such as the office block on the left are attached. The violet areas mark the

erection of the last building block next to the office and the beginning works in the periphery of the main hall. Pink areas can be found only at the edges of the buildings as well as on the parking lot at the upper right corner of the construction site. They indicate the last installations before the completion of the whole complex. An oblique aerial photo of the completed factory is displayed in Figure 23c. The single parts of the building as well as the parking lots can be well distinguished. Additionally, they correspond exactly to the signatures that can be found in the summed-up change diagram in Figure 25. Some positive changes along the roads are visible as well. Those again refer to vehicles that were slightly shifted because of their motion in contrast to the surrounding landscape. Causing strong changes in the backscatter they are captured by the automated approach, but one can easily mask them out by reducing the image to the borders of the construction site. The same goes for the few changes detected on agricultural land in the surrounding of the new factory hall.

5. Conclusions

Novel image representations—especially the Curvelet coefficients—have proven a high potential for SAR image processing. The advantage of describing structures apparent in an image instead of single pixel values enables the distinction between significant image content and noise. Therefore, image comparison in terms of change detection is transported for the first time directly to the Curvelet coefficient domain. Out of the resulting differential Curvelet coefficients the ones holding distinct information can easily be selected by statistical methods. Artifacts in the enhanced images—that normally are quite frequent with novel image representations—are avoided by applying a newly developed weighting function that guarantees a smooth transition from coefficients kept unchanged and coefficients removed. The changes detected by the automated method are compared to the changes detected by today's standard techniques, as well as by five human SAR interpreters. As a simple quality check already proved that even the results of human interpreters are highly variable, the majority of all five classifications is calculated as reference map. Although the three automated methods do not differ that much in numbers, checking the location of the missed hits and false alarms in a visual quality assessment documents that the standard techniques cannot compete with our new Curvelet-based approach in terms of reliability, *i.e.*, removing false alarms by small-scale noise-induced changes. Above all, the automated Curvelet-based approach still is much faster than any human interpreter. In order to underline the suitability of this approach time series of TerraSAR-X high resolution spotlight data over a construction site are processed. The change images clearly show the progress from one acquisition to the other. Especially for progress monitoring, it is convenient to display all new objects together in one single diagram showing their first appearance during the construction activities. Hence, construction stages become evident. As this approach is completely independent of any manual interaction, it is qualified for automated processing chains. Supplementary, being able to deliver reliable change detection results in a very short time, the Curvelet-based change detection excels as suitable tool for any rapid change detection application. The Curvelet approach designed for structural changes thus has proven its suitability in predominantly man-made environments while its usability for large-scale laminar changes expected in natural environments still has to be further investigated though preliminary studies reported surprisingly good results [36]. The inclusion of multi-layer images like multi-polarized SAR acquisitions promises not only robust change

detection results, but even a detailed change characterization which has already shown a high potential in wetland monitoring, *cf.*, previous studies in [37]. At last, this innovative Curvelet-only-based image comparison technique—though developed and presented in the context of SAR remote sensing—turned out to be suitable for numerous other robust change detection purposes based on any kind of noisy image data during preliminary studies.

Acknowledgments

Author contribution

Andreas Schmitt is the principal author of this paper. The technique presented here is one facet of his research activities at the German Aerospace Center (DLR) over the last few years. Birgit Wessel and Achim Roth supervised his work.

Conflicts of Interest

The authors declare no conflict of interest.

References and Notes

1. Carincotte, C.; Derrode, S.; Bourennane, S. Unsupervised change detection on SAR images using fuzzy hidden Markov chains. *IEEE Trans. Geosci. Remote Sens.* **2006**, *44*, 432–441.
2. Gamba, P.; Dell'Acqua, F.; Lisini, G. Change detection of multitemporal SAR data in urban areas combining feature-based and pixel-based techniques. *IEEE Trans. Geosci. Remote Sens.* **2006**, *44*, 2820–2827.
3. Dekker, R.J. SAR Change Detection Techniques and Applications. In Proceedings of 25th EARSeL Symposium on Global Developments in Environmental Earth Observation from Space, Porto, Portugal, 6–11 June 2005.
4. Liu, W.; Yamazaki, F. Urban Monitoring and Change Detection of Central Tokyo Using TerraSAR-X Images. In Proceedings of 2011 IEEE International Geoscience and Remote Sensing Symposium, Vancouver, BC, Canada, 24–29 July 2011.
5. Liao, M.; Jiang, L.; Lin, H.; Huang, B.; Gong, J. Urban change detection based on coherence and intensity characteristics of SAR imagery. *Photogramm. Eng. Remote Sens.* **2008**, *74*, 999–1006.
6. Derrode, S.; Mercier, G.; Pieczynski, W. Unsupervised Change Detection in SAR Images Using a Multicomponent HMC Model. In Proceedings of the Second International Workshop on Multi-temp'03, Ispra, Italy, 16–18 July 2003.

7. Bouyahia, Z.; Benyoussef, L.; Derrode, S. Change detection in synthetic aperture radar images with a sliding hidden Markov chain model. *J. Appl. Remote Sens.* **2008**, doi:10.1117/1.2957968.

8. Conradsen, K.; Nielsen, A.A.; Schou, J.; Skriver, H. A test statistic in the complex Wishart distribution and its application to change detection in polarimetric SAR data. *IEEE Trans. Geosci. Remote Sens.* **2003**, *41*, 4–19.

9. Erten, E. Information Theory of Multi-Temporal SAR Systems with Application to Motion Detection and Change Detection. Ph.D. Thesis, Technical University of Berlin, Berlin, Germany, November 2010.

10. Ban, Y.; Yousif, O.A. Multitemporal spaceborne SAR data for urban change detection in China. *IEEE Sel. Top. Appl. Earth Obs. Remote Sens.* **2012**, *5*, 1087–1094.

11. Shan, Z.; Wang, C.; Zhang, H.; Wu, F. Change Detection in Urban Areas with High Resolution SAR Images Using Second Kind Statistics based G0 Distribution. In Proceedings of 2010 IEEE International Geoscience and Remote Sensing Symposium, Honolulu, HI, USA, 25–30 July 2010.

12. Auer, S.; Balz, T.; Becker, S.; Bamler, R. 3D SAR simulation of urban areas based on detailed building models. *Photogramm. Eng. Remote Sens.* **2010**, *76*, 1373–1384.

13. Balz, T. SAR Simulation based Change Detection with High-Resolution SAR Images in Urban Environments. *Int. Arch. Photogramm. Remote Sens. Spat. Inf. Sci.* **2004**, *35*, 472–477.

14. Romero, R.; Sanz-Marcos, J.; Carrasco, D.; Moreno, V.; Valero, J.L.; Lafitte, M. SAR Superresolution Change Detection for Security Applications. In Proceedings of Envisat Symposium 2007, Montreux, Switzerland, 23–27 April, 2007.

15. Cui, S.; Datcu, M. Statistical wavelet subband modeling for multi-temporal SAR change detection. *IEEE J. Sel. Top. Appl. Earth Obs. Remote Sens.* **2012**, *5*, 1095–1109.

16. Bovolo, F.; Bruzzone, L. A detail-preserving scale-driven approach to change detection in multitemporal SAR images. *IEEE Trans. Geosci. Remote Sens.* **2005**, *43*, 2963–2972.

17. Candès, E.J.; Donoho, D.L. Curvelets—A Surprisingly Effective Nonadaptive Representation for Objects with Edges. In Proceedings of the International Conference on Curves and Surfaces, Saint-Malo, France, 1–7 July 1999.

18. Atto, A.M.; Trouvé, E.; Berthoumieu, Y.; Mercier, G. Multidate divergence matrices for the analysis of SAR image time series. *IEEE Trans. Geosci. Remote Sens.* **2013**, *51*, 1922–1936.

19. Schmitt, A. Change Detection Using Multi-Temporal and Multi-Polarized Radar Acquisitions. Ph.D. Thesis, Karlsruhe Institute of Technology (KIT), Karlsruhe, Germany, December 2012.

20. Schmitt, A.; Wendleder, A.; Wessel, B.; Roth, A. Comparison of Alternative Image Representations in the Context of SAR Change Detection. In Proceedings of 2010 IEEE International Geoscience and Remote Sensing Symposium, Honolulu, HI, USA, 25–30 July 2010.

21. Schmitt, A.; Wessel, B.; Roth, A. Curvelet approach for SAR image denoising, structure enhancement, and change detection. *Int. Arch. Photogramm. Remote Sens. Spat. Inf. Sci.* **2009**, *38-3/W4*, 151–156

22. Hazewinkel, M. *Encyclopedia of Mathematics*; Kluwer Academic Publishers: Dordrecht, The Netherlands, 2001.

23. Donoho, D.L.; Duncan, M.R. Digital Curvelet Transform: Strategy, Implementation, and Experiments. In Proceedings of Aerosense 2000, Wavelet Applications VII, Orlando, FL, USA, 24–28 April 2000; pp. 12–29.

24. Ulaby, F.T.; Dobson, M.C. *Handbook of Radar Scattering Statistics for Terrain*; Artech House: Norwood, MA, USA, 1989.

25. Starck, J.-L.; Candès, E.J.; Donoho, D.L. The curvelet transform for image denoising. *IEEE Trans. Image Process.* **2002**, *11*, 670–684.

26. Sveinsson, J.R.; Benediktsson, J.A. Combined Wavelet and Curvelet Denoising of SAR Images Using TV Segmentation. In Proceedings of the IEEE International Geoscience and Remote Sensing Symposium, Barcelona, Spain, 23–28 July 2007.

27. Ali, A.-D.; Swami, P.D.; Singhai, J. Modified curvelet thresholding algorithm for image denoising. *J. Comput. Sci.* **2010**, *6*, 18–23.

28. Staudt, V. Effects of Window Functions Explained by Signals Typical to Power Electronics. In Proceedings of the IEEE 8th International Conference on Harmonics and Quality of Power, Athens, Greece, 14–18 October 1998.

29. Roth, A.; Huber, M.; Kosmann, D. Geocoding of TerraSAR-X data. *Int. Arch. Photogramm. Remote Sens. Spat. Inf. Sci.* **2004**, *35*, 840–844.

30. Schmitt, A.; Wessel, B.; Roth, A. Curvelet-based change detection on SAR images for natural disaster mapping. *Photogramm. Fernerkund. Geoinf.* **2010**, *6*, 463–474.

31. Demanet, L. CurveLab 2.1.2; 2008. Curvelet.org. Available online: http://curvelet.org (accessed on 6 March 2014).

32. Cluster Applied Remote Sensing. TerraSAR-X Ground Segment—Basic Product Specification Document. Available online: http://sss.terrasar-x.dlr.de/pdfs/TX-GS-DD-3302.pdf (accessed on 20 August 2013).

33. Kuan, D.T.; Sawchuk, A.A.; Strand, T.C.; Chavel, P. Adaptive restoration of images with speckle. *IEEE Trans. Acoust Speech Signal Process.* **1987**, *35*, 373–383.

34. Joseph Vögele AG. Available online: http://www.voegele.info/de/ueber_uns/historie/werksumzug/baufortschritt/baufortschritt_1.html (accessed on 6 June 2013).

35. Kirscht, M. Estimation Of Velocity, Shape, and Position of Moving Objects with SAR. In Proceedings of the 4th International Airborne Remote Sensing Conference and Exhibition, Ottawa, ON, Canada, 21–24 June 1999.

36. Brisco, B.; Schmitt, A.; Murnaghan, K.; Kaya, S.; Roth, A. SAR polarimetric change detection for flooded vegetation. *Int. J. Digit. Earth* **2013**, *6*, 103–114.

37. Schmitt, A.; Brisco, B. Wetland monitoring using the curvelet-based change detection method. *Water* **2013**, *5*, 1036–1051.